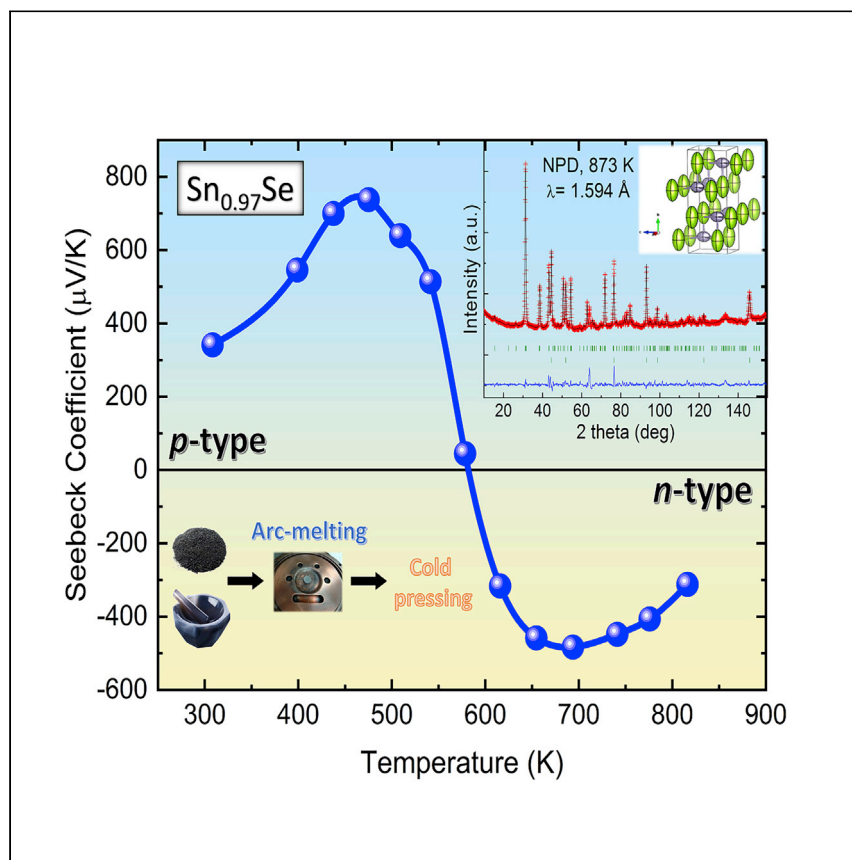


Article

High-Performance *n*-type SnSe Thermoelectric Polycrystal Prepared by Arc-Melting



SnSe single crystals are known to exhibit notable thermoelectric performance. Gainza et al. show that a fast and inexpensive arc-melting procedure followed by simple cold-pressing produces *n*-type thermoelectric pellets. Interestingly, at lower temperatures, this material is *p*-type, with a transition around 580 K to *n*-type.

Javier Gainza, Federico Serrano-Sánchez, João E.F.S. Rodrigues, ..., José Luis Martínez, José Antonio Alonso, Norbert M. Nemes

j.gainza@csic.es

HIGHLIGHTS

n-type SnSe polycrystalline pellets are prepared by a fast arc-melting synthesis

ZT ~1.8 of polycrystalline SnSe approaches that of *n*-type single crystals

Low thermal conductivity without removing strongly oxidized grain boundaries



Article

High-Performance *n*-type SnSe Thermoelectric Polycrystal Prepared by Arc-Melting

Javier Gainza,^{1,9,10,*} Federico Serrano-Sánchez,¹ João E.F.S. Rodrigues,¹ Yves Huttel,¹ Oscar J. Dura,² Michael M. Koza,³ María Teresa Fernández-Díaz,³ Juan J. Meléndez,^{4,5} Bence G. Márkus,^{6,7} Ferenc Simon,^{6,7} José Luis Martínez,¹ José Antonio Alonso,¹ and Norbert M. Nemes^{1,8}

SUMMARY

Tin selenide (SnSe) has notable thermoelectric properties, yet stable *n*-type polycrystalline SnSe is difficult to synthesize. Here, polycrystalline SnSe is easily prepared by arc-melting as robust pellets, with thermoelectric properties repeatably changing to negative Seebeck-coefficient above 580 K reaching a figure of merit ~ 1.8 at 816 K. DC conductivity changes 4 orders of magnitude with temperature, whereas microwave conductivity increases only 4-fold, confirming the effects of oxidized grain boundaries. Effects of ambient oxygen exposure are probed by X-ray photoelectron spectroscopy. Neutron powder diffraction reveals 3% Sn deficiency. Inelastic neutron scattering shows phonon spectrum consistent with *ab initio* calculations and reported Raman spectra, but with higher-energy modes strongly softened at higher temperatures. We thereby provide insight on undoped *n*-type polycrystalline SnSe that reveals high-performance at high temperature, being a suitable peer material for *p*-type SnSe.

INTRODUCTION

Thermoelectrics, which enable direct conversion of heat to electricity, can become key materials for solving the current and future energy issues worldwide. The performance of these thermoelectric materials can be assessed by the figure of merit, $ZT = S^2\sigma T/\kappa_t$, where S , T , σ , and κ_t are the Seebeck-coefficient, the electrical conductivity, the absolute temperature, and the total thermal conductivity, respectively. This total thermal conductivity includes the lattice (κ_l) and electronic contributions (κ_e).¹ Although commercial devices have $ZT \sim 1$,^{2,3} and state-of-the-art materials have surpassed ZT of 2,^{4,5} much research still remains to develop a competitive thermoelectric device. A particularly difficult challenge is to find both *p*- and *n*-type materials with similar thermoelectric and thermomechanical properties, in order to build durable thermoelectric elements.^{5,6}

Chalcogenides, well-known compounds such as PbTe,^{7,8} GeTe,^{4,9,10} or Bi₂Te₃,^{2,11} have long been among the best performing thermoelectric materials due to their complex electronic structures and low intrinsic lattice thermal conductivity. These compounds have been widely investigated using diverse approaches in order to improve their thermoelectric performance.^{12–15} Nevertheless, lead toxicity and tellurium shortage thwart these high-performance thermoelectric materials.

Recently, promising thermoelectric properties were reported in undoped *p*-type SnSe single crystals,^{16,17} generating great expectations.^{18–22} Despite exhaustive

¹Instituto de Ciencia de Materiales de Madrid ICMM-CSIC, Calle Sor Juana Inés de la Cruz, 3, Cantoblanco, 28049 Madrid, Spain

²Departamento de Física Aplicada and INEI, Universidad de Castilla-La Mancha, 13071 Ciudad Real, Spain

³Institut Laue-Langevin, C.S. 20156, 38042 Grenoble Cedex 9, France

⁴Departamento de Física, Universidad de Extremadura, Badajoz 06006, Spain

⁵Instituto de Computación Científica Avanzada de Extremadura, Badajoz 06006, Spain

⁶Department of Physics, Budapest University of Technology and Economics and MTA-BME Lendület Spintronics Research Group (PROSPIN), P.O. Box 91, 1521 Budapest, Hungary

⁷Laboratory of Physics of Complex Matter, École Polytechnique Fédérale de Lausanne, Lausanne 1015, Switzerland

⁸GFMC, Departamento de Física de Materiales, Universidad Complutense de Madrid, 28040 Madrid, Spain

⁹Twitter: @JGainza8

¹⁰Lead Contact

*Correspondence: j.gainza@csic.es

<https://doi.org/10.1016/j.xcpr.2020.100263>



research following these outstanding results,^{23–25} it has been difficult to reproduce similar high thermoelectric performance in polycrystalline tin selenide.^{26–30} In turn, even better thermoelectric performance was predicted in *n*-type SnSe.^{31,32} However, doping SnSe with donor or acceptor elements is more challenging than in other IV–VI chalcogenide semiconductors, like PbTe or GeTe. Thus, obtaining an *n*-type SnSe is not straightforward.³³

Polycrystalline SnSe has been thoroughly studied in recent years: by optimization of the carrier concentration via traditional doping strategies,^{27,28,34–37} analyzing nano-structuration effects,^{38–41} the influence of Sn and Se vacancies on the thermoelectric properties,^{42–47} and oxygen exposure on the transport properties.^{48,49} Minimizing oxidation is crucial to attain good thermoelectric properties in SnSe; Lee et al.⁵⁰ reported a near-single-crystal *p*-type thermoelectric performance in polycrystalline SnSe after a chemical reduction process, and Zhang et al.⁵¹ concluded that the oxygen behaves as a hole-like doping agent because of the electron capture by the oxygen due to its large electronegativity.

In this work, we describe the arc-melting synthesis of SnSe as well as its structural characterization by neutron powder diffraction (NPD). We use inelastic neutron scattering (INS) to show that locally the lattice dynamics matches earlier reports of SnSe single crystals. X-ray photoelectron spectroscopy (XPS) is used to investigate the surface oxidation by air exposure. In contrast to earlier reports by some of us on the thermoelectric properties below room temperature⁵² with very high resistivity, we show the complete characterization of resistivity, Seebeck-coefficient, and thermal conductivity above 300 K for arc-melted tin selenide. We find a transition from *p*-type to *n*-type behavior around 580 K. We compare DC and microwave conductivity to reveal the effects of oxidized grain boundaries on the electronic transport. Notwithstanding the influence of the oxygen exposure, we obtain a high figure of merit (up to $ZT \sim 1.8$) above 800 K, where SnSe invariably shows its best thermoelectric efficiency.

RESULTS AND DISCUSSION

Structural Characterization

NPD experiments were essential to characterize the structural features of our SnSe specimen, and in particular to decouple the occupancy and displacement factors. Figure 1 compares the laboratory X-ray diffraction (XRD) pattern from the pressed pellet used for phase purity characterization (Figure 1A), the synchrotron X-ray diffraction (SXRD) taken from rotating powder (Figure 1B), and the NPD pattern (Figure 1C), as the corresponding Rietveld plots. Trials to refine the structure from SXRD data were unsuccessful, hampered by a strong preferred orientation that could not be modeled, which is actually even worse than for laboratory XRD. The present neutron data were free of these effects, helped by the large volume of loosely packed powder in vanadium cylinders; additionally, the absence of form factors enabled reaching a wide region of the reciprocal space, thus permitting a successful structure refinement.

It is well known that SnSe crystallizes, at room temperature, in the GeS structural type, defined in the orthorhombic *Pnma* space group (No 62) $Z = 4$. Basically, it consists of corrugated layers of SnSe_3 and SeSn_3 pyramids, forming a covalent framework by sharing corners (Figure 1C, inset). Adjacent layers are held together by weaker van der Waals forces, thus making this selenide easily cleavable. We used the model described in Serrano-Sánchez et al.⁵² to refine the crystal structure.

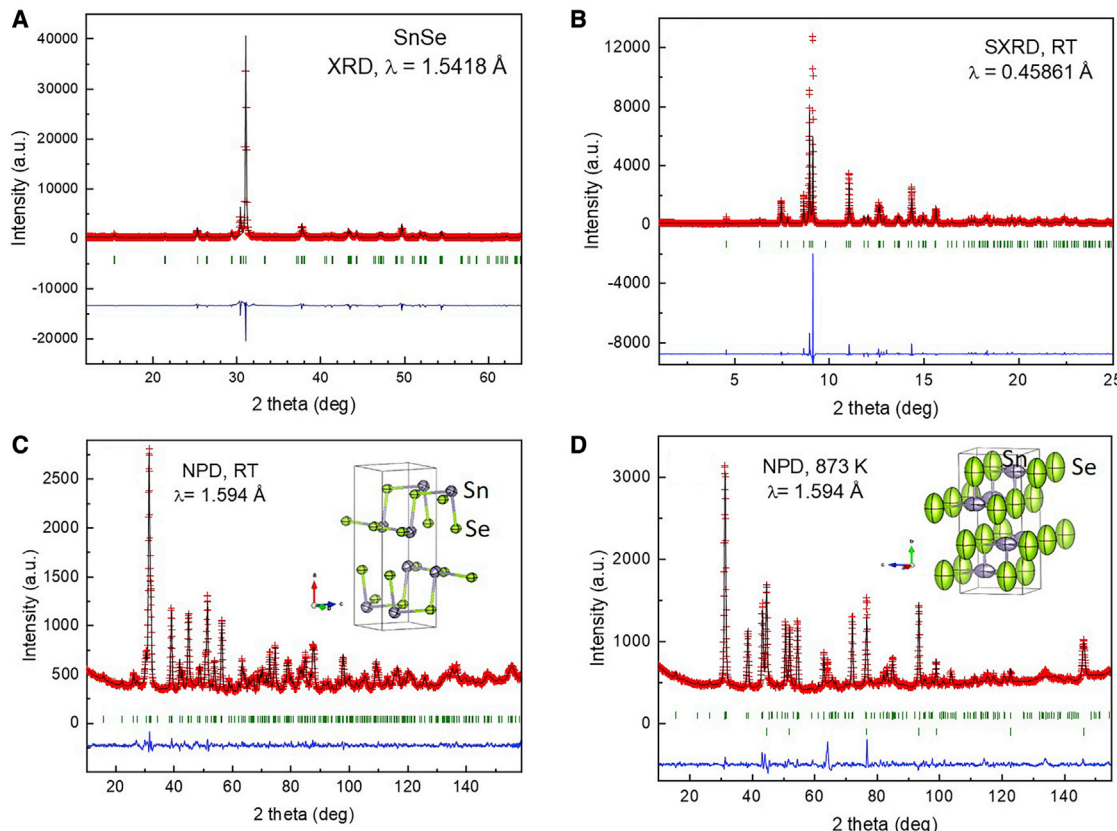


Figure 1. Crystal Structure

- (A) XRD pattern for arc-melted SnSe, Rietveld-refined in the space group *Pnma*.
- (B) Rietveld plot from SXRD data, showing a strong preferred orientation effect, which prevents the structural refinement.
- (C) Rietveld plot from NPD data at room temperature (RT), displaying a good agreement between observed (crosses) and calculated (full line) profiles, with the difference below. The tick lines correspond to the allowed Bragg reflections. The inset illustrates a view of the SnSe crystal structure at RT, highlighting the anisotropic ellipsoids of both elements (with 95% probability).
- (D) Rietveld plot from NPD data at 853 K. The second row of Bragg reflections corresponds to Fe from the sample holder. The inset illustrates the high-T orthorhombic SnSe crystal structure (*Cmcm* space group), with large cigar-shaped anisotropic ellipsoids for Se atoms.

Both Sn and Se atoms are placed at $4d(x, \frac{1}{4}, z)$ positions; the atomic parameters are listed in Table S1. The occupancy factors of Sn (with respect to Se fixed to unity) gave a significant departure from the full stoichiometry, yielding the crystallographic formula as $\text{Sn}_{0.969(7)}\text{Se}$. An excellent agreement was reached between observed and calculated profiles, as shown in Figure 1C. The refined unit-cell parameters at room temperature (RT), $a = 11.5073(6)$, $b = 4.15539(17)$, $c = 4.4445(2) \text{ \AA}$, and $V = 212.52(2) \text{ \AA}^3$, are consistent with those previously reported.⁵² The displacement ellipsoids of the atoms in the crystal structure are illustrated in the inset of Figure 1C. Prolate-type slightly elongated ellipsoids are observed for both elements; the root-mean-square (RMS) displacements for Sn are 0.14, 0.13, and 0.16 \AA along the three crystallographic directions, and 0.11, 0.12, and 0.15 \AA for Se, showing that the atoms thermally vibrate within the layers; it is believed that the lone electron pairs of both elements are directed to the interlayer space.⁵³ The SnSe_3 pyramids have Sn–Se bond lengths of $2.7970(15)(\times 2) \text{ \AA}$ and $2.753(2) \text{ \AA}$; the shorter interlayer Sn–Se distances are $3.3409(17) \text{ \AA}$.

Above $T_t \approx 795 \text{ K}$, the structure experiences a phase transition to a higher symmetry polymorph. The NPD pattern at 853 K shows a full transition to this TII-type structure

Table 1. Surface Composition

Sputt. time (min)	At.%				
	O 1s	C 1s	Sn 3d	Se 3d	Sn/Se
"fresh" SnSe					
0	14.3	62.2	12.6	10.9	1.1
30	4.9	52.9	23.0	19.2	1.2
60	4.9	51.1	24.6	19.4	1.3
"aged" SnSe					
0	26.6	54.9	11.8	6.7	1.8
20	13.8	52.1	19.7	14.4	1.4
35	10.9	53.2	20.1	15.8	1.3

Surface composition of the as-prepared tin selenide ("fresh" SnSe) and the tin selenide pellet kept at laboratory conditions for 1 week ("aged" SnSe). Also shown is the surface composition for these samples after the argon bombardment during different times inside the XPS chamber. Here, the elemental surface quantifications were extracted from Survey spectra of all the pellets. Sputt., sputtering. At.%, atomic percentage in %.

(space group *Cmcm*), which was modeled with both Sn and Se atoms at $4c(0, \frac{1}{4}, z)$ positions. At 853 K, the unit-cell parameters are $a = 4.3190(5)$, $b = 11.7268(11)$, $c = 4.3019(4)$ Å. The refined parameters are included in [Table S2](#); the goodness of the fit is illustrated in [Figure 1D](#). The thermal ellipsoids of Sn atoms become flattened, with RMS displacement values of 0.11, 0.21, and 0.25 Å along the three axes, whereas for Se the ellipsoids are cigar-shaped, with greater RMS values of 0.23, 0.45, and 0.23 Å. A view of the crystal structure is displayed as an inset in [Figure 1D](#). We emphasize that the highest thermoelectric performance occurs in this structural type, above 800 K, as described below.

XPS Characterization

In order to investigate the effect of oxygen exposure, surface chemistry studies in SnSe were carried out by means of XPS. The XPS spectra were acquired from two samples: from the as-prepared SnSe pellet (referred to as "fresh") and a second pellet kept at laboratory conditions (exposed to air at room temperature) for 1 week (referred to as "aged"). Both samples were also sputtered using argon ions (Ar^+) for different times with survey spectra collected, as listed in [Table 1](#) containing the surface quantification of the elements O, C, Sn, and Se in atomic percentage. The sputtering process was employed in order to check that the oxidation is predominant at the sample surface, as discussed next.

The fresh SnSe pellet was rapidly placed in the XPS chamber after cold-pressing in order to reduce the aging process. The elemental surface quantification of fresh SnSe pellet exhibited an excess of tin at the surface (i.e., the Sn/Se ratio was around 1.1), which partially agrees with the tin deficiency determined from bulk techniques, such as NPD. This ratio increases from 1.1 up to 1.3 after the argon bombardment, which shows a preferential sputtering of the Se atoms, as already reported in literature.⁵⁴ In [Figure 2A](#), the high-resolution photoelectron spectra at Sn 3d core levels are displayed. The fitting of the XPS spectrum for the fresh sample revealed the presence of six components (three components for the $\text{Sn } 3d_{5/2}$ and another three for the $\text{Sn } 3d_{3/2}$) that could be assigned to SnSe (56.4%), SnO_2 (41.4%), and Sn^0 (2.2%) at 494.1, 495.1, and 492.5 eV Sn 3d_{3/2} core levels,⁵⁴ respectively. For the fresh pellet as sputtered inside the XPS chamber for 60 min (named "fresh-sputtered-60"), the photoemission spectrum at Sn 3d core levels displayed a strong reduction of the SnO_2 component from 41.4% to 9.2%, revealing the surface nature of the oxide.

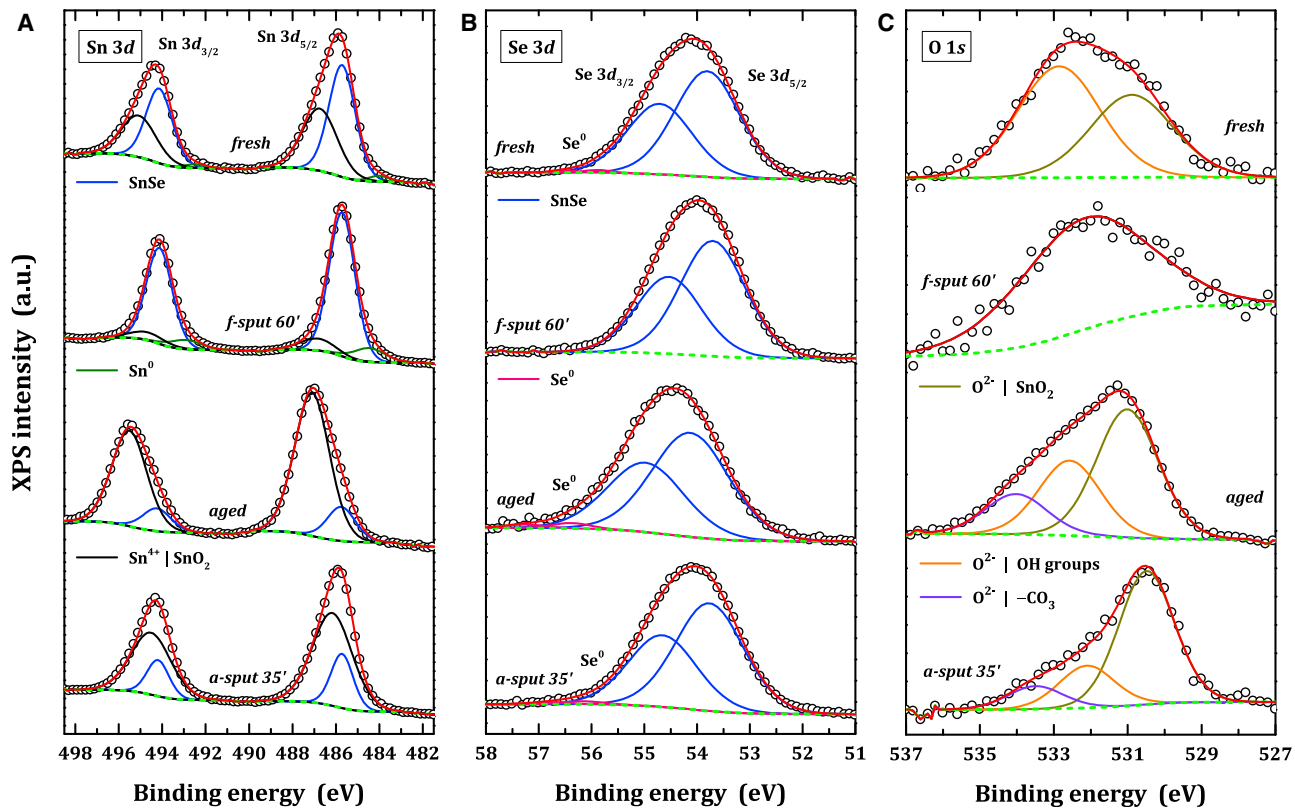


Figure 2. Surface Oxides

Photoelectron spectra of the SnSe pellets (vertically shifted for clarity): (A) Sn 3d, (B) Se 3d, and (C) O 1s. Open circles and red lines denote the experimental and fitted data, respectively. Solid lines represent the components for fitting process using Shirley background (dotted light green lines). During the XPS experiments, two SnSe samples were employed: the as-prepared pellet (named “fresh”) and a second pellet kept at laboratory conditions for 1 week (named “aged”). Both pieces were sputtered inside the XPS chamber for different times, as listed in Table 1, in order to probe the oxidation effect on the grain surfaces.

In Figure 2B, the high-resolution photoelectron spectra at Se 3d core levels are shown. In the fitting process, four components were found for the fresh SnSe (two for the Se $3d_{5/2}$ and another two for the Se $3d_{3/2}$), attributed to SnSe (98.9%) and Se⁰ (1.1%) at 53.8 and 55.9 eV Se $3d_{5/2}$ core levels⁵⁴, respectively. For the fresh-sputtered-60’ sample, no components of Se not bounded to tin selenide were found after the argon bombardment. Figure 2C depicts the high-resolution O 1s XPS spectra for the fresh and fresh-sputtered-60’ samples. In the case of the fresh sample, two components at 530.9 and 532.8 eV could be identified and ascribed to oxygen bound to tin and OH groups at the surface,^{55,56} respectively. After the sputtering with argon, the spectrum exhibited a hard to ascribe single low intensity and broad peak at 532.2 eV.

Otherwise, the aged SnSe pellet has almost 83.8% of oxidized surface (SnO_2 at 495.5 eV Sn $3d_{3/2}$ core level) against 16.2% of SnSe (at 494.2 eV Sn $3d_{3/2}$ core level), as extracted from the photoelectron spectra at Sn 3d core levels of Figure 2A. The elemental surface quantification of aged SnSe exhibited the Sn/Se ratio near 1.8, which means that the surface oxidation due to SnO_2 shields the photoelectron signal from Se element. After the argon bombardment, the Sn/Se ratio decreased from 1.8 down to 1.3 in 35 min of sputtering time and, therefore, almost recovering the original value of 1.1 for fresh SnSe pellet. The argon “sputtered aged” SnSe sample

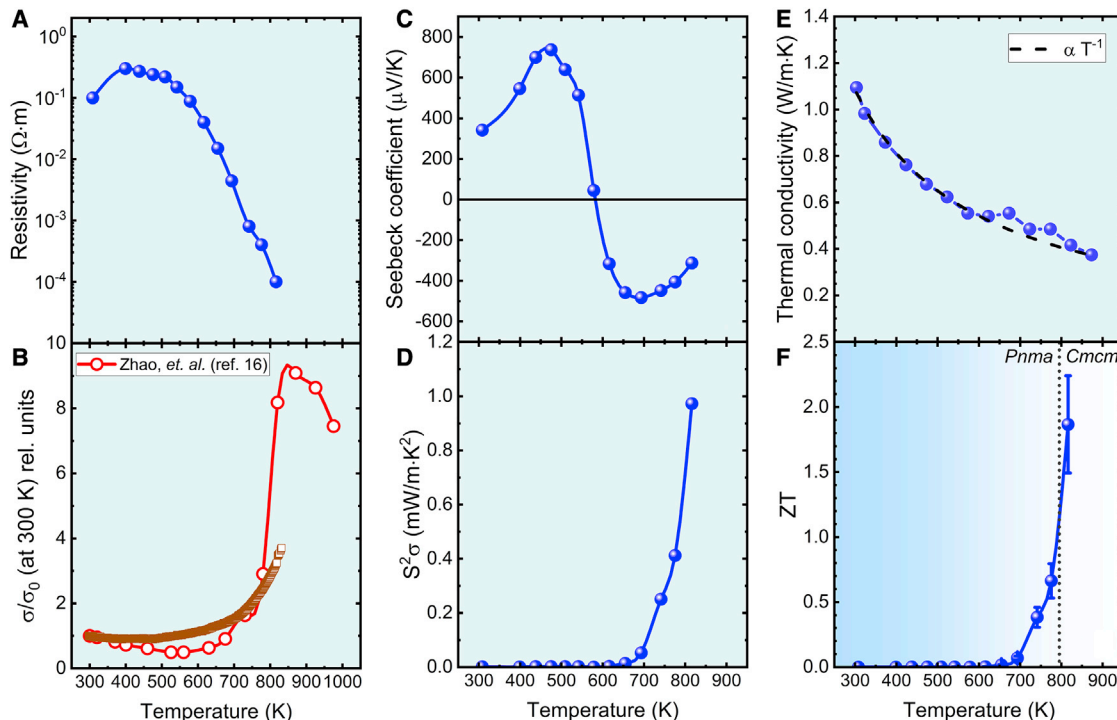


Figure 3. Thermoelectric Properties

Temperature dependence of the thermoelectric properties of SnSe polycrystal prepared by arc-melting: (A) electrical resistivity, (B) relative change of the microwave conductivity (squares), and, for comparison, the DC conductivity of a SnSe single crystal as extracted from Zhao et al.¹⁶ (circles), (C) Seebeck-coefficient, (D) power factor, (E) total thermal conductivity, and (F) ZT figure of merit. The vertical dotted line indicates the structural transition. The uncertainty of the figure of merit is around 20%.

See also Figures S1, S2, and S3.

(named “aged-sputtered-35”) depicted only a reduction from 83.8% to 75.4% in the SnO_2 quantity at the surface. It denotes that the oxygen exposure of SnSe pellet can generate grains with surface oxide layer throughout the sample that may affect the electrical conductivity due to an insulator barrier between grains.⁵⁷

In Figure 2B, the high-resolution photoelectron spectra at Se 3d core level of both aged SnSe and aged-sputtered-35’ exhibit a slight variation in the percentage of Se^0 (2.5% and 1.6%, respectively). It can be understood as a sputtering effect of only tin elements in aged SnSe, which corroborates that the SnO_2 is mainly distributed on the grain surface of SnSe samples that were exposed to oxygen in laboratory conditions. Also, the O 1s photoelectron spectrum of aged SnSe starts to exhibit a third component at 534.0 eV probably due to the $-\text{CO}_3$ surface species.⁵⁴ Therefore, XPS results confirmed the tendency for tin to segregate to the grain surfaces in polycrystalline tin selenide. SnSe pellet is very sensitive to surface oxidation, which may hinder the electrical properties of polycrystalline samples.⁵¹

Transport Measurements

The effects of the surface oxide of the grains can be unveiled by comparing the DC and microwave conductivities (Figures 3A and 3B). The DC resistivity shows a dramatic, near exponential drop of 3–4 orders of magnitude between 400 and 800 K in Figure 3A. This, when analyzed in terms of a thermal activation energy, indicates a transport gap of around 1.03 eV, somewhat larger than the band gap of SnSe.^{53,58} The gap value is consistent with the acceptor character of the oxygen in SnSe,⁵¹

which may induce local electrostatic repulsions at the grain boundaries. Consequently, the band structure changes locally at the grain boundaries to accommodate the acceptor levels associated with the oxide layer, which results in a slight gap opening. This interpretation is reinforced by comparison to the microwave conductivity in **Figure 3B**, measured using aged SnSe powder sealed in 4-mm quartz tubes under helium atmosphere. Microwave conductivity (σ) measures the intrinsic, intragrain properties and is not affected by the surface oxide barriers. This is valid in the limit when there is no grain-to-grain conductivity and is justified by the low DC conductivity at room temperature (for details, see [Experimental Procedures](#)). The method only provides relative values of σ , and data shown in **Figure 3B** are relative to room temperature. Surprisingly, the microwave conductivity behaves very similar to the DC conductivity reported on high quality SnSe single crystals (compared in **Figure 3B** with red lines from Zhao et al.¹⁶) and not at all like that expected from **Figure 3A**. This proves that the local conductivity in our sample grains matches the intrinsic properties of SnSe, whereas the DC resistivity of pressed pellets of fine grains is obscured by the grain boundary effects. The microwave conductivity only shows a 4-fold increase between 400 and 800 K, in stark contrast to the 4 orders of magnitude of the DC conductivity. Notice the small resistivity increase (microwave conductivity decrease) just above 300 K in both **Figures 3A** and **3B**, also reported for single crystals.¹⁶

All the thermoelectric parameters for one arc-melted SnSe sample are shown in **Figure 3** as a function of increasing temperature: the resistivity in **Figure 3A**, the Seebeck-coefficient in **Figure 3C**, the power factor in **Figure 3D**, the thermal conductivity in **Figure 3E**, and the resulting figure of merit in **Figure 3F** with maximum value of $ZT \sim 1.8$. The temperature dependence of the Seebeck-coefficient shows an atypical change of sign around 580 K and a high temperature value of $\sim -350 \mu\text{V/K}$. All the thermoelectric properties were measured along the pressing direction, where previous reports show a higher ZT .^{27,39,60} The electronic transport measurements were performed just after the synthesis process, in order to avoid the possible oxidation of the samples (fresh). Every undoped SnSe sample studied (whether fresh or aged, see **Figure 4**) shows a sudden *p*- to *n*-type transition at a temperature around 550–600 K. This behavior has been already reported before, at a similar temperature, in Se-deficient tin selenide,⁴³ but not in the stoichiometric or Sn-deficient compound.^{44,45} However, several anomalies have been observed around this temperature in other polycrystalline SnSe.^{26,42,61,62} Moreover, some theoretical studies have previously predicted this change of sign.^{31,63,64} Indeed, Loa et al.⁶³ attributed the rapid decrease and sign reversal of the Seebeck coefficient to the onset of the bipolar conductivity, which is amplified and shifted to lower temperatures by a rapid reduction of the gap at high temperatures. The strong preferred orientation of our polycrystalline tin selenide (as we can see in **Figure 1B**), may also be related to the observed *p* to *n* transition of this layered material.⁶³ The corresponding *p*-type charge carrier concentration (n_H) at room temperature is $\sim 1.28 \times 10^{18} \text{ cm}^{-3}$ as extracted from the Hall-effect measurement. This carrier density is slightly higher than other reported data for tin-deficient single-crystal SnSe⁴⁶ (around $4 \times 10^{17} \text{ cm}^{-3}$), but below that reported for tin-deficient polycrystalline SnSe^{45,65} (around $1 \times 10^{19} \text{ cm}^{-3}$). Considering transport dominated by acoustic phonons,⁶⁶ this carrier density would correspond to an effective mass of $0.49 m_e$ and a mobility of $\sim 0.5 \text{ cm}^2 \times V^{-1} \times s^{-1}$ at room temperature. This effective mass is similar to that obtained by Zhao et al.¹⁷ using a single-band model ($0.47 m_e$), although this value is not valid to explain the experimental data. On the other hand, the mobility is low compared to the $25 \text{ cm}^2 \times V^{-1} \times s^{-1}$ reported for single crystals,¹⁶ although it is much closer to the reported mobility of $4 \text{ cm}^2 \times V^{-1} \times s^{-1}$ for the reduced polycrystalline SnSe.⁵⁰

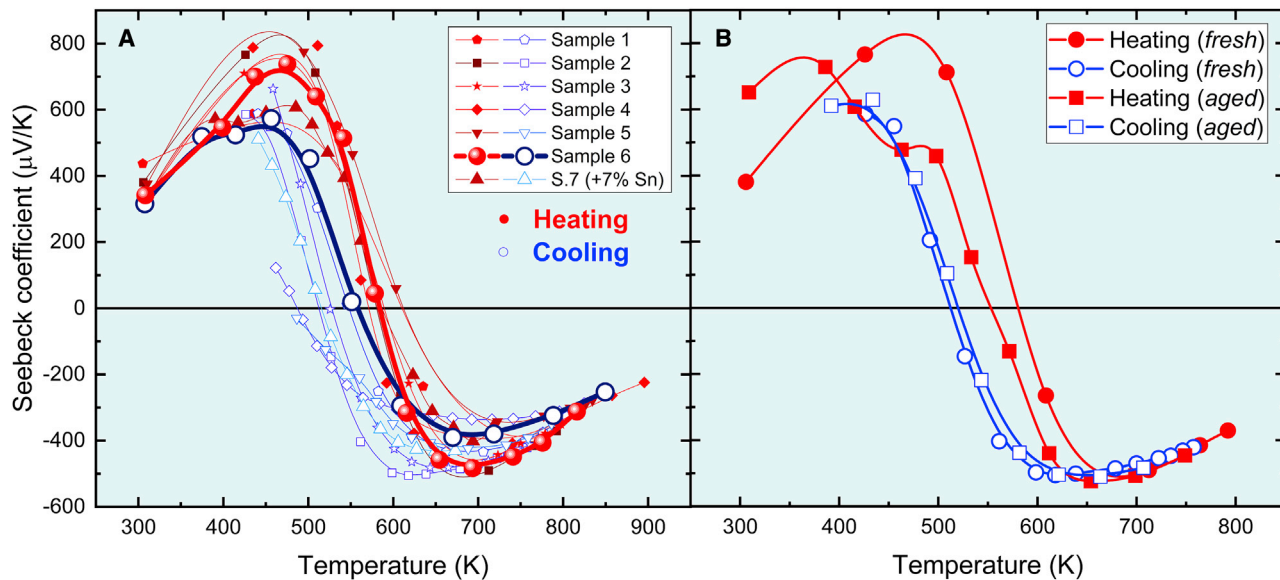


Figure 4. Reproducibility

Comparison of the temperature dependence of the Seebeck-coefficient of (A) several arc-melted SnSe polycrystals measured upon heating (red) and cooling (blue), and (B) just after synthesis (circles) and after 10 months exposed to ambient air (squares). Lines are guides for the eye. See also Figures S4 and S5.

This low mobility explains the poor room-temperature thermoelectric performance of the tin selenide samples of this study.⁵²

The reproducibility of the high temperature behavior of Seebeck-coefficient is demonstrated in Figure 4. Data from six nominally identical arc-melted SnSe polycrystals, and an additional one where 7% extra Sn was intentionally added to the precursor in an unsuccessful attempt to counteract the structural Sn-deficiency produced by arc-melting are shown in Figure 4A. These samples were measured right after the synthesis and cold-pressing (equivalent to the fresh state) upon heating and also cooling, to check for repeatability in each. Figure S1 shows their Seebeck-coefficient and DC resistivity. Furthermore, one sample was measured again, after it was left in ambient air in the laboratory for 10 months (Figure 4B). The Seebeck-coefficient shows quite a bit of variation below the p- to n- transition around 550–600 K between samples, for heating and cooling of each sample, and for the fresh and aged state of the same sample. However, all the Seebeck-coefficients tend toward a uniform high temperature behavior, slowly decreasing from a peak value of around $-500 \mu\text{V/K}$ above the transition to around $-350 \mu\text{V/K}$ at 800 K, where the high thermoelectric performance is observed. This result is in accordance to that predicted by Loa et al.,⁶³ who calculated a Seebeck coefficient of $\sim -400 \mu\text{V/K}$ around 800 K in the direction perpendicular to the layers.

Ab Initio Calculations

This anomalous behavior, in particular the p- to n- transition, may be explained on the basis of several concurrent effects; in fact, some theoretical studies have predicted before this change of sign.^{31,63,64} More precisely, Loa et al.⁶³ attributed the rapid decrease and sign reversal of the Seebeck coefficient to the onset of bipolar conductivity, amplified and shifted to lower temperatures by the gap shrinkage at around 700 K, and to the marked anisotropy of SnSe. In our case, the strong preferred orientation of the polycrystalline tin selenide samples (as we can see in

Figure 1B) may relate the observed *p* to *n* transition of this layered material to the prediction by Loa et al.⁶³ Another effect that may help to explain the observed trend, as Loa et al.⁶³ themselves concede, is the contribution of defect levels located close to the edge of the conduction band; note that the existence of these defects may well reduce the gap, which is therefore consistent with the previous analysis.

In this regard, one could try to understand the role played by the surface oxide layer and the aforementioned tin deficiency on the transport properties of SnSe by a set of *ab initio* calculations coupled with solutions of the Boltzmann transport equation; this is a methodology that has been shown to yield good results in this system.⁶⁷ Such a study would require computational resources well beyond our capabilities, mainly due to the need to build large supercells to mimic the defect configurations. However, we may still extract some insights from theoretical predictions about defective SnSe reported elsewhere.³² Indeed, oxygen behaves as acceptor in SnSe, as we have already mentioned,⁵¹ and acceptor impurities at Sn sites of the SnSe lattice may be stable under some conditions. This is the case of the In_{Sn} defect, for instance, which yields an impurity level around 0.03 eV below the bottom of the conduction band. Thus, a system with acceptor impurities at Sn sites would behave as *p*-type at temperatures below that of ionization of the acceptor impurities—that is around 400 K for In_{Sn}—, but would exhibit a transition to *n*-type behavior at higher temperatures. Another possibility involves unfilled Sn vacancies. A comparison of the calculated electronic density of states for both stoichiometric and tin-deficient SnSe (Sn_{0.94}Se) shows a broad defect-band right above the valence band for the tin-deficient SnSe,⁶⁸ reproduced in **Figure S8**, possibly contributing to the behavior of the Seebeck-coefficient. This is relevant in light of the Rietveld-refined occupancy factor for our tin deficient SnSe with a Sn/Se ratio of 0.97.

Finally, we note that the Seebeck-coefficient is asymmetric, with a higher absolute maximum below 550 K, in the *p*-type regime. This asymmetry may be associated with an energy filtering (EF) effect^{69,70} at the oxide layer of the grain boundaries. EF consists in the reduction of the flow of minority charge carriers by high-energy potential barriers associated with some defects. The suppression of the bipolar effect does not reduce significantly the electrical conductivity, because the propagation of the majority charge carriers is promoted, but it increases the Seebeck-coefficient. EF has been modeled for a number of defect configurations.^{71–74} Narducci et al.⁷⁵ have modeled the EF modification of the Seebeck-coefficient within the relaxation-time approximation for the Boltzmann equation as an average weighted by the electrical conductivity:

$$S = -\frac{3m^*}{2e^3 T} \langle \epsilon - \epsilon_F \rangle_\sigma, \quad (1)$$

where m^* and e are the effective mass and charge of the charge carriers and ϵ_F is their Fermi energy. **Equation 1** shows that an asymmetric variation of the Fermi energy with the temperature, as in a *p*-type to *n*-type transition, may explain an asymmetric shape of the S curve. This asymmetry has indeed been observed experimentally,^{76,77} although it is generally considered weak. In any case, a much more detailed computational study, which ideally should be coupled with experimental structural data, would be required to elucidate the previous issues.

The power factor, from DC conductivity and Seebeck-coefficient, is calculated as $S^2 \sigma$ (**Figure 3D**). The sudden increase at 700 K reflects the near exponential decrease of the resistivity, falling below $10^{-3} \Omega \times m$ at that temperature. This sharp increase in the power factor has been reported before,^{28,29,36,43} but here the maximum power

factor of $\sim 1.0 \text{ mW} \times \text{m}^{-1} \times \text{K}^{-2}$ at 816 K in a pressed pellet approaches that originally reported for single crystalline SnSe ($\sim 1.0 \text{ mW} \times \text{m}^{-1} \times \text{K}^{-2}$ at 800–900 K),¹⁶ and exceeds that of chemically reduced *p*-type SnSe polycrystals, with a maximum value of $0.7 \text{ mW} \times \text{m}^{-1} \times \text{K}^{-2}$ at $\sim 770 \text{ K}$.⁵⁰ At $\sim 816 \text{ K}$, our power factor is also higher than other tin deficient tin selenides, like that reported by Wei et al.,⁴⁴ achieving around $0.6 \text{ mW} \times \text{m}^{-1} \times \text{K}^{-2}$ for the $\text{Sn}_{0.95}\text{Se}$. The highest power factor of Figure 3D is also observed for another sample, as shown in Figures S1 and S2.

Thermal Conductivity

High *ZT* in SnSe is mainly attributed, in addition to the ultra-high power factor, to the ultra-low thermal conductivity (Figure 3E) due to the strongly anharmonic bonding in this compound.^{16,33} In this work, thermal conductivity was determined from the thermal diffusivity. Because of the relatively high resistivity at low temperature, the electronic contribution to the total thermal conductivity becomes appreciable only above 750 K, with $0.03 \text{ W} \times \text{m}^{-1} \times \text{K}^{-1}$ at 773 K (Figure S3). Therefore, the measured values almost entirely reflect the lattice contribution. At room temperature, the thermal conductivity is $\sim 1.09 \text{ W} \times \text{m}^{-1} \times \text{K}^{-1}$, while above 700 K it has an ultra-low value ($< 0.5 \text{ W} \times \text{m}^{-1} \times \text{K}^{-1}$),²³ reaching $0.37 \text{ W} \times \text{m}^{-1} \times \text{K}^{-1}$ at 873 K. This behavior is similar to other reported data for polycrystalline undoped SnSe,^{27,43,44} although it does not reach the record-low value of $0.23 \text{ W} \times \text{m}^{-1} \times \text{K}^{-1}$ achieved for single crystals.¹⁶ The thermal conductivity decreases as T^{-1} approximately (dashed line), which is an indication of phonon scattering dominated by Umklapp processes.¹⁹

Previously reported *ab initio* calculations⁶⁷ have shown that, indeed, the electronic contribution to the thermal conductivity is negligible at temperatures below 500 K. Besides, the analysis of the phonon spectrum reveals that a key parameter to understand heat conduction in SnSe is the critical length λ^* at which the transition between the ballistic (i.e., collision-free) and diffusive conduction regimes takes place. In particular, if the grain size $d >> \lambda^*$, phonons are scattered within the grains. The critical length (that is anisotropic) varies with temperature; at 300 K it is around $0.9\text{--}1.0 \mu\text{m}$, thus comparable to the grain size of our samples, but it shrinks to around 400 nm at 600 K. As a consequence, SnSe polycrystals and single crystals should exhibit comparable thermal conductivities at high temperatures, where the condition $d >> \lambda^*$ is easily fulfilled, in good agreement with our results. Furthermore, the thermal conductivity is essentially the same along and perpendicular to the pressing direction, despite the strong texturing (Figure S6). At low temperature, thermal conduction is instead ruled by grain boundary phonon scattering.^{67,68}

The high power factor together with this ultra-low thermal conductivity result in an outstanding figure of merit of *ZT* $\sim 1.5\text{--}1.8$ at 816 K, as can be seen in Figure 3F. Similar high values have been reported so far only in doped polycrystalline SnSe^{28,30,44,78}; however, as far as we know, this is the highest *ZT* reported to date in *n*-type undoped polycrystalline SnSe.^{30,35,38,79,80} As Chen et al.⁸¹ point out, “an ideal SnSe-based thermoelectric material should be described as polycrystalline SnSe composed by nanograins with single-crystal-like anisotropy and optimized *n*.” This work can pave the way to move forward in this concept.

INS

The detailed phonon spectrum of SnSe is important to understand the ultra-low thermal conductivity. An analysis of the anisotropic displacement parameters (ADPs) can give a rough estimate of the vibrational energies and were identified before from NPD.⁸² The highly anisotropic thermal ellipsoids of the ADPs revealed strong

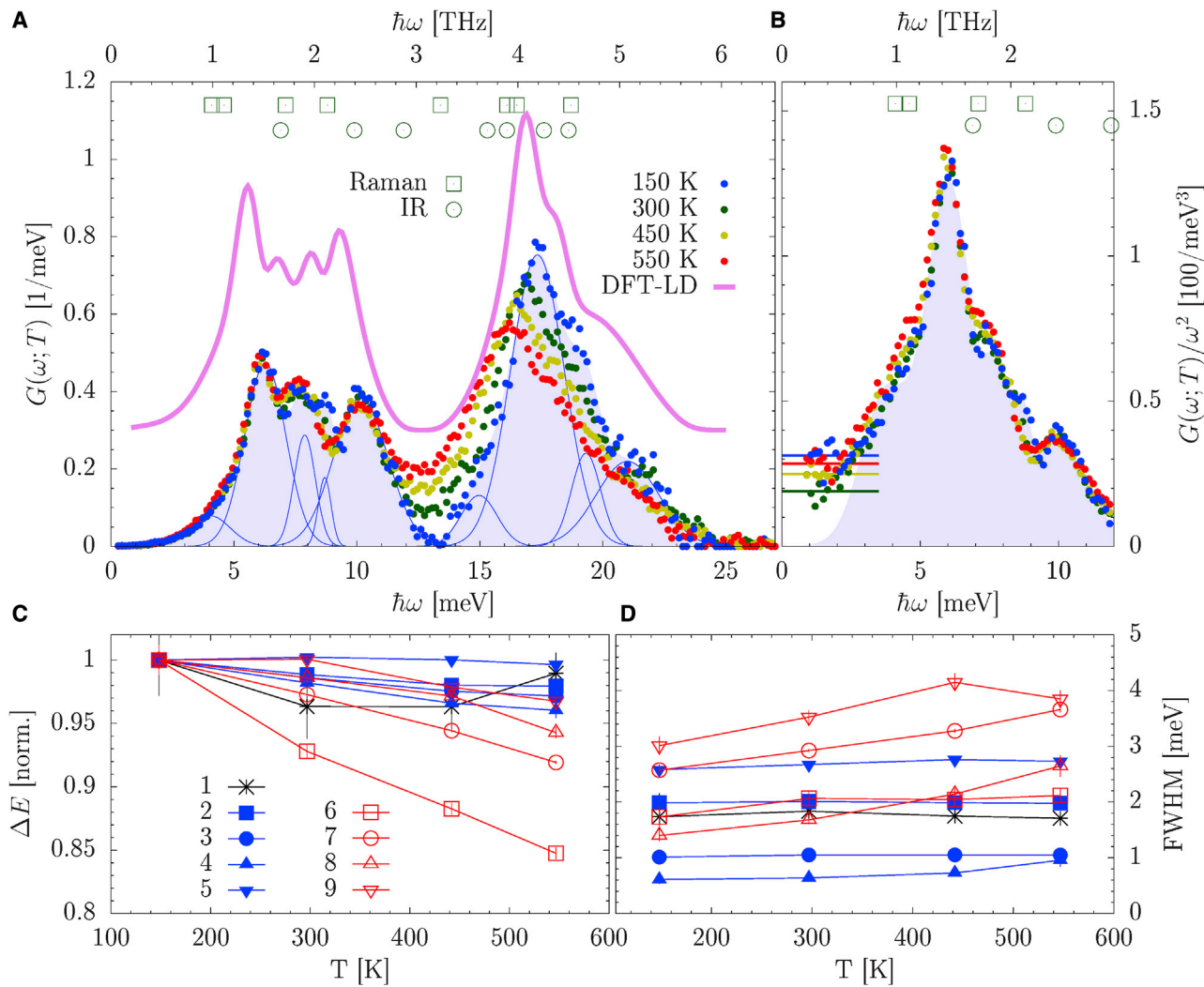


Figure 5. Phonons

Temperature dependence of the generalized phonon density of states $G(\omega; T)$ of SnSe from inelastic neutron scattering (INS).

(A) $G(\omega; T)$ (filled points) and results from fits with 9 Gaussians (thin solid lines) to the data at 150 K. The shaded area represents the total signal of the fit. For comparison, data from DFT-based lattice dynamics calculations (DFT-LD) are shown by the thick solid line, upshifted by 0.3.

(B) $G(\omega; T)/\omega^2$ highlighting the characteristic spectral texture in the low-energy range. Solid horizontal lines indicate the low-energy level associated with long-wavelength phonons. For comparison, measured room temperature Raman and IR modes are indicated in (A) and (B) by open symbols adapted from Chandrasekhar et al.⁸³

(C) Energy shift of the 9 identified peaks in (A) from their values at 150 K.

(D) Full width at half maximum (FWHM) of the peaks derived from Gaussian fits. The peaks are numbered according to their increasing eigenfrequency. Low- and high-energy peaks are discriminated with blue and red color, respectively.

anharmonicity and permitted to assign up to three modes between 7–8 meV to the movement of Sn and another three around 9–11 meV to that of Se.

Here, we report the INS and identify several vibrational energies, some with important softening at high temperature (Figure 5). In order to quantify characteristic modes and their temperature dependence, the generalized density of states (GDOS) have been approximated by 9 Gaussians through χ^2 fits in the energy range between 2.5 and 26 meV. Thereby, the relative intensities of the Gaussians were determined only at 150 K and kept fixed at those values for any data at higher

T . Thus, the relative number of excitations represented by the Gaussians were appointed constant and only their positions and widths were matched. The relative energy shifts and the full widths at half maximum of the Gaussians are presented in Figures 5C and 5D. The intensities and eigenenergies computed at 150 K are listed in Table S3. Figure 5B presents the lower energy part of the same data scaled as $G(\omega; T)/\omega^2$. The indicated low-energy levels (Figure 5B) associated with long-wavelength phonons lead to estimated temperature dependent sound velocity and Debye temperature, as given in Table S4.

The higher effective scattering power of Se (~ 0.11 barns [$1e^{-24} \text{ cm}^2$] $\times \text{amu}^{-1}$) in comparison to Sn (~ 0.04 barns $\times \text{amu}^{-1}$) shifts the spectral weight toward the higher energy modes determining the strong intensity above 13 meV than expected from earlier first principle calculations.⁸⁴ Because the present experiment sampled the inelastic response in an extended momentum range, any vibrational excitation of low-dispersion contributes to $G(\omega; T)$ with a high signal. Thus, peaks identified in the $G(\omega; T)$ do not correspond exclusively to Γ -point modes. We compare the measured phonon spectrum with *ab initio* calculations in Figure 5A. The *ab initio* dataset has been broadened by a Gaussian convolution whose width approximates the energy resolution in the applied experimental setup. The calculations match the experiment remarkably well in terms of the number of peaks, their widths, and intensities, with only a slight mismatch in the energy shifts.

We also find a stunning match between some prominent, fitted peaks of our GDOS and results from Raman and IR experiments reported in the literature.^{85,86} For convenience, we indicate in Figures 5A and 5B the room temperature experimental results by Chandrasekhar et al.⁸³ This match does not only hold for the eigenfrequencies of the peaks at low T but comprises as well their renormalization upon heating as best evidenced by the Raman experiments of Liu et al.⁸⁵ In general, peaks around 15–18 meV whose energies correspond to B_{3g} and A_{2g} Γ -point excitations show a particularly strong T dependence which we approximate to $6 \mu\text{eV} \times \text{K}^{-1}$ close to the results of the Raman studies. This correspondence holds as well for other peaks in particular in the low-energy range dominated by Sn amplitudes⁸⁴ and for the highest energy modes being less responsive to T changes.^{82,83} The characterization of the peak of lowest energy located around 4 meV that is formed by lowest energy Γ -point excitations is hampered by the acoustic tail in the $G(\omega; T)$.²⁴ We cannot identify a particular temperature rescaling within the reliability of the fit results, as highlighted by the mismatch in the low-energy part in Figure 5B.

We presented a synthesis of polycrystalline SnSe by an arc-melting technique followed by cold pressing as robust pellets. NPD reveals 3% structural Sn-deficiency and confirms the well-known *Pnma*-to-*Cmcm* structural transition. The structure, surface chemical composition, lattice dynamics, thermal conductivity, and comparison of the electrical DC and microwave conductivities reveal that the material consists of grains, albeit deficient in Sn, with properties inherently similar to single crystals, but separated by surface oxide layers as grain boundaries. XPS measurements corroborate that oxygen from ambient atmosphere alters the tin selenide grain surfaces over time. The phonon spectrum, as measured by Inelastic Neutron Spectroscopy, is in good agreement with the calculated *ab initio* spectrum of SnSe. The Seebeck-coefficient of arc-melted SnSe switches to negative above 580 K, and the thermoelectric figure of merit ZT reaches ~ 1.8 at 816 K. We thereby obtain a high-performance *n*-type thermoelectric behavior at high temperature in (undoped) polycrystalline SnSe. This arc-melted material could be a suitable peer to the *p*-type polycrystalline tin selenide for the manufacturing of high-performance commercial thermoelectric devices.

EXPERIMENTAL PROCEDURES

Resource Availability

Lead Contact

Further information and requests for resources and reagents should be directed to and will be fulfilled by the Lead Contact, Javier Gainza (j.gainza@csic.es).

Materials Availability

This study did not generate new unique reagents.

Data and Code Availability

The authors declare that data supporting the findings of this work are available within the article and the Supplemental Information. Any other data are available from the Lead Contact upon reasonable request.

Reagents

The following reagents were used as obtained, unless otherwise noted: Mixtures of nominal stoichiometric amounts of Sn (Alfa Aesar, 99.8%) and Se (Alfa Aesar, 99.999%) were ground, pelletized, and molten under Ar atmosphere in a water-cooled Cu crucible, resulting in intermetallic ingots.

Synthesis

SnSe specimens were obtained as compact pellets, where intimate contact between grains is already established, directly from an Edmund Buhler MAM-1 mini-arc furnace. These pellets are directly cold pressed in a dye (without grinding them to powder), by doing so the density of each pellet increases (around 90% of the crystallographic value, by mass and volume measurement) and the dimensions are easily measured and reproduced. We can do so thanks to the malleability of this material, easily deformable. We emphasize that, as shown by refinement of the NPD, this synthesis preferentially yields Sn-deficient SnSe, contrary to expectations based on the larger volatility of Se. Elemental analysis by total reflection X-ray fluorescence (TXRF) shows 2% Sn deficiency. This preference cannot even be counteracted by intentionally loading up to 7% extra Sn into the starting material. The extra Sn may evaporate or end up within/around the sample, but not within the grains of SnSe structure, and rapidly oxidize.

Compacting Ingots

Part of the as-grown ingots were ground to powder for structural analysis and the remaining part was cold-pressed to obtain a pellet that was used for transport measurements. A consolidation process such as spark plasma sintering (SPS) yields higher densities but promotes the spreading of the oxide films on grain boundaries throughout the pellets, which is detrimental for the thermoelectric properties,⁵⁰ so this technique was not considered in this study.

Synchrotron X-Ray Powder Diffraction

The material science and powder diffraction (MSPD)-diffractometer beamline at CELLS-ALBA synchrotron (Barcelona, Spain) was employed to collect the pattern, using the high-angular resolution mode (MAD set-up) with an incident beam of 27 keV energy ($\lambda = 0.45861 \text{ \AA}$).⁸⁷ The polycrystalline powder was contained in rotating quartz capillaries of 0.7 mm diameter. The SXRD pattern was collected at room temperature.

NPD

Good quality NPD patterns were collected for SnSe in the high-resolution D2B neutron diffractometer at ILL (Grenoble-France), with the high-flux mode and a counting time of 2 h. Approximately 1.5 g of sample was contained in a vanadium

holder. A wavelength of 1.594 Å was selected from a Ge monochromator; the measurement temperatures were 295 K (RT) and 853 K. For the data collection above room temperature, a furnace with vanadium resistors, working in vacuum, was utilized. All the patterns were refined by the Rietveld method,⁸⁸ using the FULLPROF refinement program.⁸⁹ A pseudo-Voigt function was chosen to generate the line shape of the diffraction peaks. No regions were excluded in the refinement. In the final run, the following parameters were refined from the high-resolution D2B data: scale factor, background coefficients, zero-point error, unit-cell parameters, pseudo-Voigt corrected for asymmetry parameters, positional coordinates, and anisotropic displacement factors for Sn and Se atoms. The coherent scattering lengths for Sn and Se atoms were 6.225 and 7.970 fm, respectively.

XPS

Samples were loaded in an ultra-high vacuum XPS chamber (base pressure in the low 10^{-10} mbar) equipped with a hemispherical electron energy analyzer (SPECS Phobos 100 spectrometer) and an Al $K\alpha$ (1486.29 eV) X-ray source. Survey-spectra were recorded using an energy step of 0.5 eV and a pass-energy of 40 eV, while specific core level spectra (Sn 3d, Se 3d, O 1s, and C 1s) were acquired with an energy step of 0.1 eV and a pass-energy of 20 eV. Initial fittings by taking into account the C 1s core level at 285 eV,⁹⁰ as a calibration of the absolute binding energies, were unsuccessful due to the absence of adventitious carbon in the sputtered samples (see Figure S7). In this way, the absolute BE was obtained based on the Sn 3d_{5/2} core level at 485.7 eV for all the XPS spectra; this assumption made the fittings more reliable in view of the elemental quantification and core level positions for the remaining elements. Data processing was performed with CasaXPS software.

Thermoelectric Properties

All the thermoelectric properties were measured along the pressing direction, where previous reports show a higher ZT.^{27,39,60} Seebeck-coefficient and resistivity measurements were carried out in high vacuum (10^{-6} mbar) in a homemade apparatus.⁹¹ The DC resistivity, simultaneously with the Seebeck-coefficient, was measured in a 4-probe configuration, in high vacuum, in a home-built setup following the design of Iwanaga et al.⁹² Details of the implementation of this measurement can be found in Gainza et al.⁹¹

Microwave Conductivity

Temperature-dependent microwave conductivity is determined⁹³ by monitoring the quality factor of a cylindrical TE₀₁₁ microwave cavity with and without the sample. Microwave conductivity⁵⁹ measures the intrinsic, intragrain properties and is not affected by the surface oxide barriers. This is valid in the limit when there is no grain-to-grain conductivity and justified by the low DC conductivity at room temperature. In the so-called penetration limit, when the microwaves fully penetrate into the sample (grain size smaller than the skin-depth), the observed microwave loss, L , is proportional to the local conductivity.^{59,94} Even the lowest resistivity is above $10^{-4} \Omega \times m$, implying a penetration depth at 10 GHz of $\sim 100 \mu m$, still much larger than the grain size of our SnSe, on the order of 1 μm .⁶⁸ Then, temperature-dependent microwave conductivity is obtained from $\sigma(T) \sim 1/Q_{sample} - 1/Q_0$, where Q_0 is the quality factor of the empty cavity.⁹¹

Hall Effect and Charge Carrier Density

The Hall-coefficient, $R_H = 1/n_H e$, below 400 K was measured using the 4-probe resistivity option of a PPMS (Quantum Design) with an alternating DC current of $I = 5mA$ in a van der Pauw geometry, by sweeping the magnetic field between $\pm 9T$.

Thermal Conductivity

Thermal conductivity was determined from the thermal diffusivity (α) using a Linseis LFA 1000 instrument by a laser-flash technique, as $\kappa = \alpha \times C_p \times d$, where C_p is the specific heat and $d = 5.6 \text{ g cm}^{-3}$ is the sample density. The specific heat was calculated using the Dulong-Petit equation, $C_p = 252 \text{ J} \times \text{kg}^{-1}\text{K}^{-1}$.

INS

The INS data were collected at the cold-neutron spectrometer IN6-Sharp at the European neutron source Institut Laue-Langevin in Grenoble, France.⁹⁵ Approximately 12 g of sample was used (obtained from 6 consecutive syntheses). An incident wavelength of 4.14 Å and the inelastic-focusing mode with the target energy of 7 meV was utilized to cover a sufficiently large energy-momentum phase space with best resolution in the energy range of interest. Standard corrections for empty can, detectors' efficiency and its energy dependence, frame overlap, as well as self-attenuation effects were carried out with the software package LAMP.⁹⁶ The corrected signal was transformed to the phonon density of states by means of the incoherent approximation⁹⁷ having applied a self-consistent multi-phonon correction algorithm MuPhoCor^{98,99} implemented in the software package LAMP. The one-phonon generalized densities of states $G(\omega; T)$ are presented in Figure 5. Irrespective of the different scattering power of Sn and Se, which is determined by the fraction of their neutron cross sections and atomic masses, all $G(\omega; T)$ have been normalized to six phonon modes. Additional information can be found in Tables S3 and S4 and Note S2.

Ab Initio Phonon Spectrum

The density of states (DOS) and GDOS for phonons were integrated from the calculated phonon spectrum considering up to third-order anharmonic interatomic force constants (IFCs). The harmonic, second-order IFCs and the third-order anharmonic ones were calculated using the Phonopy¹⁰⁰ and ShengBTE¹⁰¹ packages, respectively. In all cases, a real-space $2 \times 2 \times 2$ supercell approach ($2 \times 3 \times 6$ k-mesh) with finite displacements and a cutoff range for the interactions of 6.5 Å was used; only the Γ -point was used in the Brillouin zone. According to previous studies,⁶⁷ van der Waals corrections according to the DFT-D method were explicitly used.¹⁰²

SUPPLEMENTAL INFORMATION

Supplemental Information can be found online at <https://doi.org/10.1016/j.xcpr.2020.100263>.

ACKNOWLEDGMENTS

We thank ILL and ALBA personnel for making all facilities available for the neutron and synchrotron experiments. Calculations have been performed in the Cyfronet Computer Centre using Prometheus computer, which is a part of the PL-Grid Infrastructure. We are grateful for support from the Spanish Ministry of Science, Innovation and Universities (MICINN) (MAT2017-84496-R and PGC2018-094763-B-I00), the Junta de Extremadura (Spain) (IB16013, partially funded by FEDER), the National Research Development and Innovation Office of Hungary (NKFIH) (K119442 and 2017-1.2.1-NKP-2017-00001), MICINN (PRE2018-083398 to J.G.), and the Brazilian agency CAPES (Finance Code 001: 88881.171031/2018-01 to J.E.R.). J.G.: <https://orcid.org/0000-0002-1999-3116>; F.S.-S.: <https://orcid.org/0000-0002-6882-225X>; J.E.F.S.R.: <https://orcid.org/0000-0002-9220-5809>; Y.H.: <https://orcid.org/0000-0002-3683-9890>; O.J.D.: <https://orcid.org/0000-0002-4014-7555>; M.M.K.: <https://orcid.org/0000-0002-5133-8584>; M.T.F.-D.: <http://publons.com/researcher/2545716/maria-teresa-fernandez-diaz/>; J.J.M.: <https://orcid.org/0000-0003-1036-6666>; B.G.M.:

<https://orcid.org/0000-0003-1472-0482>; F.S.: <https://orcid.org/0000-0001-9822-4309>; J.L.M.: <https://orcid.org/0000-0001-9046-8237>; J.A.A.: <https://orcid.org/0000-0001-5329-1225>; N.M.N.: <https://orcid.org/0000-0002-7856-3642>.

AUTHOR CONTRIBUTIONS

J.A.A., J.L.M., and N.M.N. conceived and designed the study. J.G. and F.S.-S. synthesized the samples. J.G., J.L.M., N.M.N., and O.J.D. characterized the thermoelectric performance. J.A.A. and M.T.F.-D. carried out and analyzed the NPD. J.G., N.M.N., and M.M.K. carried out and analyzed the INS. J.E.F.S.R. and Y.H. carried out and analyzed the XPS. B.G.M. and F.S. carried out and analyzed the microwave conductivity experiment. J.J.M. performed the *ab initio* calculations. J.G. and N.M.N. coordinated the writing of the manuscript with discussion and input from all authors.

DECLARATION OF INTERESTS

The authors declare no competing interests.

Received: June 12, 2020

Revised: September 23, 2020

Accepted: October 27, 2020

Published: December 2, 2020

REFERENCES

1. Snyder, G.J., and Toberer, E.S. (2008). Complex thermoelectric materials. *Nat. Mater.* 7, 105–114.
2. Witting, I.T., Chasapis, T.C., Ricci, F., Peters, M., Heinz, N.A., Hautier, G., and Snyder, G.J. (2019). The Thermoelectric Properties of Bismuth Telluride. *Adv. Electron. Mater.* 5, 1800904.
3. Wu, Y., Chen, Z., Nan, P., Xiong, F., Lin, S., Zhang, X., Chen, Y., Chen, L., Ge, B., and Pei, Y. (2019). Lattice Strain Advances Thermoelectrics. *Joule* 3, 1276–1288.
4. Perumal, S., Samanta, M., Ghosh, T., Shenoy, U.S., Bohra, A.K., Bhattacharya, S., Singh, A., Waghmare, U.V., and Biswas, K. (2019). Realization of High Thermoelectric Figure of Merit in GeTe by Complementary Co-doping of Bi and In. *Joule* 3, 2565–2580.
5. Zebarjadi, M., Esfarjani, K., Dresselhaus, M.S., Ren, Z.F., and Chen, G. (2012). Perspectives on thermoelectrics: from fundamentals to device applications. *Energy Environ. Sci.* 5, 5147–5162.
6. Zheng, X.F., Liu, C.X., Yan, Y.Y., and Wang, Q. (2014). A review of thermoelectrics research - Recent developments and potentials for sustainable and renewable energy applications. *Renew. Sustain. Energy Rev.* 32, 486–503.
7. Heremans, J.P., Jovovic, V., Toberer, E.S., Saramat, A., Kurosaki, K., Charoenphakdee, A., Yamanaka, S., and Snyder, G.J. (2008). Enhancement of Thermoelectric Efficiency in PbTe by Distortion of the Electronic Density of States. *Science* 321, 554–557.
8. Biswas, K., He, J., Zhang, Q., Wang, G., Uher, C., Dravid, V.P., and Kanatzidis, M.G. (2011). Strained endotaxial nanostructures with high thermoelectric figure of merit. *Nat. Chem.* 3, 160–166.
9. Li, J., Chen, Z., Zhang, X., Sun, Y., Yang, J., and Pei, Y. (2017). Electronic origin of the high thermoelectric performance of GeTe among the p-type group IV monotellurides. *NPG Asia Mater.* 9, e353–e358.
10. Hong, M., Chen, Z.-G., Yang, L., Zou, Y.-C., Dargusch, M.S., Wang, H., and Zou, J. (2018). Realizing ZT of 2.3 in $\text{Ge}_{1-x-y} \text{Sb}_x \text{In}_y \text{Te}$ via Reducing the Phase-Transition Temperature and Introducing Resonant Energy Doping. *Adv. Mater.* 30, 1705942.
11. Wang, Y., Liu, W.-D., Gao, H., Wang, L.-J., Li, M., Shi, X.-L., Hong, M., Wang, H., Zou, J., and Chen, Z.-G. (2019). High Porosity in Nanostructured n-Type Bi_2Te_3 Obtaining Ultralow Lattice Thermal Conductivity. *ACS Appl. Mater. Interfaces* 11, 31237–31244.
12. Pei, Y., Wang, H., and Snyder, G.J. (2012). Band engineering of thermoelectric materials. *Adv. Mater.* 24, 6125–6135.
13. Biswas, K., He, J., Blum, I.D., Wu, C.I., Hogan, T.P., Seidman, D.N., Dravid, V.P., and Kanatzidis, M.G. (2012). High-performance bulk thermoelectrics with all-scale hierarchical architectures. *Nature* 489, 414–418.
14. Gainza, J., Serrano-Sánchez, F., Biskup, N., Nemes, N.M., Martínez, J.L., Fernández-Díaz, M.T., and Alonso, J.A. (2019). Influence of Nanostructuring on PbTe Alloys Synthesized by Arc-Melting. *Materials (Basel)* 12, 3783.
15. Pei, Y., Shi, X., LaLonde, A., Wang, H., Chen, L., and Snyder, G.J. (2011). Convergence of electronic bands for high performance bulk thermoelectrics. *Nature* 473, 66–69.
16. Zhao, L.-D., Lo, S.-H., Zhang, Y., Sun, H., Tan, G., Uher, C., Wolverton, C., Dravid, V.P., and Kanatzidis, M.G. (2014). Ultralow thermal conductivity and high thermoelectric figure of merit in SnSe crystals. *Nature* 508, 373–377.
17. Zhao, L.D., Tan, G., Hao, S., He, J., Pei, Y., Chi, H., Wang, H., Gong, S., Xu, H., Dravid, V.P., et al. (2016). Ultrahigh power factor and thermoelectric performance in hole-doped single-crystal SnSe. *Science* 351, 141–144.
18. Chang, C., Wu, M., He, D., Pei, Y., Wu, C.-F., Wu, X., Yu, H., Zhu, F., Wang, K., Chen, Y., et al. (2018). 3D charge and 2D phonon transports leading to high out-of-plane ZT in n-type SnSe crystals. *Science* 360, 778–783.
19. Jin, M., Chen, Z., Tan, X., Shao, H., Liu, G., Hu, H., Xu, J., Yu, B., Shen, H., Xu, J., et al. (2018). Charge Transport in Thermoelectric SnSe Single Crystals. *ACS Energy Lett.* 3, 689–694.
20. Qin, B., Wang, D., He, W., Zhang, Y., Wu, H., Pennycook, S.J., and Zhao, L.-D. (2019). Realizing High Thermoelectric Performance in p-Type SnSe through Crystal Structure Modification. *J. Am. Chem. Soc.* 141, 1141–1149.
21. Chang, C., Wang, D., He, D., He, W., Zhu, F., Wang, G., He, J., and Zhao, L.-D. (2019). Realizing High-Ranged Out-of-Plane ZTs in N-Type SnSe Crystals through Promoting Continuous Phase Transition. *Adv. Energy Mater.* 9, 1901334.
22. Wei, P.-C., Bhattacharya, S., Liu, Y.-F., Liu, F., He, J., Tung, Y.-H., Yang, C.-C., Hsing, C.-R., Nguyen, D.-L., Wei, C.-M., et al. (2019). Thermoelectric Figure-of-Merit of Fully Dense

- Single-Crystalline SnSe. *ACS Omega* 4, 5442–5450.
23. Chang, C., Tan, G., He, J., Kanatzidis, M.G., and Zhao, L.D. (2018). The Thermoelectric Properties of SnSe Continue to Surprise: Extraordinary Electron and Phonon Transport. *Chem. Mater.* 30, 7355–7367.
 24. Li, C.W., Hong, J., May, A.F., Bansal, D., Chi, S., Hong, T., Ehlers, G., and Delaire, O. (2015). Orbitally driven giant phonon anharmonicity in SnSe. *Nat. Phys.* 11, 1063–1069.
 25. Serrano-Sánchez, F., Nemes, N.M., Dura, O.J., Fernandez-Díaz, M.T., Martínez, J.L., and Alonso, J.A. (2016). Structural phase transition in polycrystalline SnSe: A neutron diffraction study in correlation with thermoelectric properties. *J. Appl. Cryst.* 49, 2138–2144.
 26. Sassi, S., Candolfi, C., Vaney, J.B., Ohorodniichuk, V., Masschelein, P., Dauscher, A., and Lenoir, B. (2014). Assessment of the thermoelectric performance of polycrystalline p-type SnSe. *Appl. Phys. Lett.* 104, 212105.
 27. Chen, C.L., Wang, H., Chen, Y.Y., Day, T., and Snyder, G.J. (2014). Thermoelectric properties of p-type polycrystalline SnSe doped with Ag. *J. Mater. Chem. A Mater. Energy Sustain.* 2, 11171–11176.
 28. Zhao, Q., Qin, B., Wang, D., Qiu, Y., and Zhao, L.-D. (2020). Realizing High Thermoelectric Performance in Polycrystalline SnSe via Silver Doping and Germanium Alloying. *ACS Appl. Energy Mater.* 3, 2049–2054.
 29. Lee, Y.K., Ahn, K., Cha, J., Zhou, C., Kim, H.S., Choi, G., Chae, S.I., Park, J.H., Cho, S.P., Park, S.H., et al. (2017). Enhancing p-Type Thermoelectric Performances of Polycrystalline SnSe via Tuning Phase Transition Temperature. *J. Am. Chem. Soc.* 139, 10887–10896.
 30. Shang, P.P., Dong, J., Pei, J., Sun, F.H., Pan, Y., Tang, H., Zhang, B.P., Zhao, L.D., and Li, J.F. (2019). Highly Textured N-Type SnSe Polycrystals with Enhanced Thermoelectric Performance. *Research (Wash D C)* 2019, 925312.
 31. Kutasinski, K., Wiendlocha, B., Kaprzyk, S., and Tobola, J. (2015). Electronic structure and thermoelectric properties of n-and p-type SnSe from first-principles calculations. *Phys. Rev. B Condens. Matter Mater. Phys.* 91, 205201.
 32. González-Romero, R.L., and Meléndez, J.J. (2018). Variation of the zT factor of SnSe with doping: A first-principles study. *J. Alloys Compd.* 732, 536–546.
 33. Zhao, L.D., Chang, C., Tan, G., and Kanatzidis, M.G. (2016). SnSe: A remarkable new thermoelectric material. *Energy Environ. Sci.* 9, 3044–3060.
 34. Peng, K., Lu, X., Zhan, H., Hui, S., Tang, X., Wang, G., Dai, J., Uher, C., Wang, G., and Zhou, X. (2016). Broad temperature plateau for high ZTs in heavily doped p-type SnSe single crystals. *Energy Environ. Sci.* 9, 454–460.
 35. Li, S., Wang, Y., Chen, C., Li, X., Xue, W., Wang, X., Zhang, Z., Cao, F., Sui, J., Liu, X., and Zhang, Q. (2018). Heavy Doping by Bromine to Improve the Thermoelectric Properties of n-type Polycrystalline SnSe. *Adv. Sci. (Weinh.)* 5, 1800598.
 36. Nguyen, V.Q., Nguyen, T.H., Duong, V.T., Lee, J.E., Park, S.-D., Song, J.Y., Park, H.-M., Duong, A.T., and Cho, S. (2018). Thermoelectric Properties of Hot-Pressed Bi-Doped n-Type Polycrystalline SnSe. *Nanoscale Res. Lett.* 13, 200.
 37. Zhang, Q., Chere, E.K., Sun, J., Cao, F., Dahal, K., Chen, S., Chen, G., and Ren, Z. (2015). Studies on Thermoelectric Properties of n-type Polycrystalline SnSe_{1-x}S_x by Iodine Doping. *Adv. Energy Mater.* 5, 1500360.
 38. Cha, J., Zhou, C., Lee, Y.K., Cho, S.-P., and Chung, I. (2019). High Thermoelectric Performance in n-Type Polycrystalline SnSe via Dual Incorporation of Cl and PbSe and Dense Nanostructures. *ACS Appl. Mater. Interfaces* 11, 21645–21654.
 39. Tang, G., Wen, Q., Yang, T., Cao, Y., Wei, W., Wang, Z., Zhang, Z., and Li, Y. (2017). Rock-salt-type nanoprecipitates lead to high thermoelectric performance in undoped polycrystalline SnSe. *RSC Advances* 7, 8258–8263.
 40. Biçer, M., and Şışman, I. (2011). Electrodeposition and growth mechanism of SnSe thin films. *Appl. Surf. Sci.* 257, 2944–2949.
 41. Zhang, L., Wang, J., Sun, Q., Qin, P., Cheng, Z., Ge, Z., Li, Z., and Dou, S. (2017). Three-Stage Inter-Orthorhombic Evolution and High Thermoelectric Performance in Ag-Doped Nanolaminar SnSe Polycrystals. *Adv. Energy Mater.* 7, 1700573.
 42. Lee, S.T., Kim, M.J., Lee, G.-G., Kim, S.G., Lee, S., Seo, W.-S., and Lim, Y.S. (2017). Effects of Sn-deficiency on thermoelectric properties of polycrystalline Sn_{1-x}Se compounds. *Curr. Appl. Phys.* 17, 732–737.
 43. Li, Q., Zhang, L., Yin, J., Sheng, Z., Chu, X., Wang, F., and Zhu, F. (2018). Study on the thermoelectric performance of polycrystal SnSe with Se vacancies. *J. Alloys Compd.* 745, 513–518.
 44. Wei, W., Chang, C., Yang, T., Liu, J., Tang, H., Zhang, J., Li, Y., Xu, F., Zhang, Z., Li, J.F., and Tang, G. (2018). Achieving High Thermoelectric Figure of Merit in Polycrystalline SnSe via Introducing Sn Vacancies. *J. Am. Chem. Soc.* 140, 499–505.
 45. Dargusch, M., Shi, X.-L., Tran, X.Q., Feng, T., Somidin, F., Tan, X., Liu, W., Jack, K., Venezuela, J., Maeno, H., et al. (2019). In-Situ Observation of the Continuous Phase Transition in Determining the High Thermoelectric Performance of Polycrystalline Sn_{0.98}Se. *J. Phys. Chem. Lett.* 10, 6512–6517.
 46. Jin, M., Shi, X.-L., Feng, T., Liu, W., Feng, H., Pantelides, S.T., Jiang, J., Chen, Y., Du, Y., Zou, J., and Chen, Z.G. (2019). Super Large Sn_{1-x}Se Single Crystals with Excellent Thermoelectric Performance. *ACS Appl. Mater. Interfaces* 11, 8051–8059.
 47. Qin, B., Zhang, Y., Wang, D., Zhao, Q., Gu, B., Wu, H., Zhang, H., Ye, B., Pennycook, S.J., and Zhao, L.-D. (2020). Ultrahigh Average ZT Realized in p-Type SnSe Crystalline Thermoelectrics through Producing Extrinsic Vacancies. *J. Am. Chem. Soc.* 142, 5901–5909.
 48. de Kergommeaux, A., Faure-Vincent, J., Pron, A., de Bettignies, R., Malaman, B., and Reiss, P. (2012). Surface oxidation of tin chalcogenide nanocrystals revealed by ¹¹⁹Sn-Mössbauer spectroscopy. *J. Am. Chem. Soc.* 134, 11659–11666.
 49. Li, Y., He, B., Heremans, J.P., and Zhao, J.-C. (2016). High-temperature oxidation behavior of thermoelectric SnSe. *J. Alloys Compd.* 669, 224–231.
 50. Lee, Y.K., Luo, Z., Cho, S.P., Kanatzidis, M.G., and Chung, I. (2019). Surface Oxide Removal for Polycrystalline SnSe Reveals Near-Single-Crystal Thermoelectric Performance. *Joule* 3, 719–731.
 51. Zhang, M., Wang, D., Chang, C., Lin, T., Wang, K., and Zhao, L.-D. (2019). Oxygen adsorption and its influence on the thermoelectric performance of polycrystalline SnSe. *J. Mater. Chem. C* 7, 10507–10513.
 52. Serrano-Sánchez, F., Gharsallah, M., Nemes, N.M., Mompeán, F.J., Martínez, J.L., and Alonso, J.A. (2015). Record Seebeck coefficient and extremely low thermal conductivity in nanostructured SnSe. *Appl. Phys. Lett.* 106, 083902.
 53. Gharsallah, M., Serrano-Sánchez, F., Nemes, N.M., Mompeán, F.J., Martínez, J.L., Fernández-Díaz, M.T., Elhalouani, F., and Alonso, J.A. (2016). Giant Seebeck effect in Ge-doped SnSe. *Sci. Rep.* 6, 26774.
 54. Badrinarayanan, S., Mandale, A.B., Gunjikar, V.G., and Sinha, A.P.B. (1986). Mechanism of high-temperature oxidation of tin selenide. *J. Mater. Sci.* 21, 3333–3338.
 55. Chen, M., Wang, X., Yu, Y.H., Pei, Z.L., Bai, X.D., Sun, C., Huang, R.F., and Wen, L.S. (2000). X-ray photoelectron spectroscopy and auger electron spectroscopy studies of Al-doped ZnO films. *Appl. Surf. Sci.* 158, 134–140.
 56. Turishchev, S.Y., Chuvenkova, O.A., Parinova, E.V., Koyuda, D.A., Chumakov, R.G., Presselt, M., Schleusener, A., and Sivakov, V. (2018). XPS investigations of MOCVD tin oxide thin layers on Si nanowires array. *Results Phys.* 11, 507–509.
 57. Francisco, L.H., Rodrigues, J.E., Correr, W.R., and Hernandes, A.C. (2018). Blocking effect in promising proton conductors based on Ba₃Ca_{1.18}Nb_{1.82-x}R_xO_{9-δ} (R = Y³⁺, Gd³⁺, Sm³⁺, Nd³⁺) ordered perovskites for PC-SOFCs. *Ceram. Int.* 44, 10806–10812.
 58. Shafique, A., and Shin, Y.-H. (2017). Thermoelectric and phonon transport properties of two-dimensional IV-VI compounds. *Sci. Rep.* 7, 506.
 59. Klein, O., Donovan, S., Dressel, M., and Grüner, G. (1993). Microwave cavity perturbation technique: Part I: Principles. *Int. J. Infrared Milli. Waves* 14, 2423–2457.
 60. Tang, G., Wei, W., Zhang, J., Li, Y., Wang, X., Xu, G., Chang, C., Wang, Z., Du, Y., and Zhao, L.-D. (2016). Realizing High Figure of Merit in Phase-Separated Polycrystalline Sn_{1-x}Pb_xSe. *J. Am. Chem. Soc.* 138, 13647–13654.

61. Fu, J., Su, X., Xie, H., Yan, Y., Liu, W., You, Y., Cheng, X., Uher, C., and Tang, X. (2018). Understanding the combustion process for the synthesis of mechanically robust SnSe thermoelectrics. *Nano Energy* 44, 53–62.
62. Li, Y., Shi, X., Ren, D., Chen, J., and Chen, L. (2015). Investigation of the anisotropic thermoelectric properties of oriented polycrystalline SnSe. *Energies* 8, 6275–6285.
63. Loa, I., Popuri, S.R., Fortes, A.D., and Bos, J.W.G. (2018). Critical mode and band-gap-controlled bipolar thermoelectric properties of SnSe. *Phys. Rev. Mater.* 2, 1–7.
64. Shi, G., and Kioupakis, E. (2015). Quasiparticle band structures and thermoelectric transport properties of p-type SnSe. *J. Appl. Physiol.* 117, 065103.
65. Shi, X., Chen, Z.-G., Liu, W., Yang, L., Hong, M., Moshwan, R., Huang, L., and Zou, J. (2018). Achieving high Figure of Merit in p-type polycrystalline Sn0.98Se via self-doping and anisotropy-strengthening. *Energy Storage Mater.* 10, 130–138.
66. May, A.F., and Snyder, G.J. (2012). Introduction to Modeling Thermoelectric Transport at High Temperatures. In *Materials, Preparation, and Characterization in Thermoelectrics*, D.M. Rowe, ed. (CRC Press), pp. 1–18.
67. González-Romero, R.L., Antonelli, A., and Meléndez, J.J. (2017). Insights into the thermoelectric properties of SnSe from ab initio calculations. *Phys. Chem. Chem. Phys.* 19, 12804–12815.
68. Gainza, J., Serrano-Sánchez, F., Gharsallah, M., Carrascoso, F., Bermúdez, J., Dura, O.J., Mompean, F.J., Biskup, N., Meléndez, J.J., Martínez, J.L., et al. (2019). Evidence of nanostructuring and reduced thermal conductivity in n-type Sb-alloyed SnSe thermoelectric polycrystals. *J. Appl. Physiol.* 126, 045105.
69. Gayner, C., and Amouyal, Y. (2019). Energy Filtering of Charge Carriers: Current Trends, Challenges, and Prospects for Thermoelectric Materials. *Adv. Funct. Mater.* 30, 1901789.
70. Bahk, J.-H., Bian, Z., and Shakouri, A. (2013). Electron energy filtering by a nonplanar potential to enhance the thermoelectric power factor in bulk materials. *Phys. Rev. B Condens. Matter Mater. Phys.* 87, 075204.
71. Faleev, S.V., and Léonard, F. (2008). Theory of enhancement of thermoelectric properties of materials with nanoinclusions. *Phys. Rev. B Condens. Matter Mater. Phys.* 77, 214304.
72. Hicks, L.D., and Dresselhaus, M.S. (1993). Effect of quantum-well structures on the thermoelectric figure of merit. *Phys. Rev. B Condens. Matter Mater. Phys.* 47, 12727–12731.
73. Lee, H., Vashaee, D., Wang, D.Z., Dresselhaus, M.S., Ren, Z.F., and Chen, G. (2010). Effects of nanoscale porosity on thermoelectric properties of SiGe. *J. Appl. Physiol.* 107, 094308.
74. Scheele, M., Oeschler, N., Veremchuk, I., Peters, S.-O., Littig, A., Kornowski, A., Klinke, C., and Weller, H. (2011). Thermoelectric properties of lead chalcogenide core-shell nanostructures. *ACS Nano* 5, 8541–8551.
75. Narducci, D., Seleznova, E., Cerofolini, G., Frabboni, S., and Ottaviani, G. (2012). Impact of energy filtering and carrier localization on the thermoelectric properties of granular semiconductors. *J. Solid State Chem.* 193, 19–25.
76. Minnich, A.J., Dresselhaus, M.S., Ren, Z.F., and Chen, G. (2009). Bulk nanostructured thermoelectric materials: current research and future prospects. *Energy Environ. Sci.* 2, 466.
77. Zide, J.M.O., Vashaee, D., Bian, Z.X., Zeng, G., Bowers, J.E., Shakouri, A., and Gossard, A.C. (2006). Demonstration of electron filtering to increase the Seebeck coefficient in In0.53 Ga0.47 As/In0.53 Ga0.28 Al0.19 As superlattices. *Phys. Rev. B Condens. Matter Mater. Phys.* 74, 205335.
78. Shi, X., Wu, A., Feng, T., Zheng, K., Liu, W., Sun, Q., Hong, M., Pantelides, S.T., Chen, Z.G., and Zou, J. (2019). High Thermoelectric Performance in p-type Polycrystalline Cd-doped SnSe Achieved by a Combination of Cation Vacancies and Localized Lattice Engineering. *Adv. Energy Mater.* 9, 1803242.
79. Ge, Z., Qiu, Y., Chen, Y., Chong, X., Feng, J., Liu, Z., and He, J. (2019). Multipoint Defect Synergy Realizing the Excellent Thermoelectric Performance of n-Type Polycrystalline SnSe via Re Doping. *Adv. Funct. Mater.* 29, 1902893.
80. Shi, X.-L., Zheng, K., Liu, W.-D., Wang, Y., Yang, Y.-Z., Chen, Z.-G., and Zou, J. (2018). Realizing High Thermoelectric Performance in n-Type Highly Distorted Sb-Doped SnSe Microplates via Tuning High Electron Concentration and Inducing Intensive Crystal Defects. *Adv. Energy Mater.* 8, 1800775.
81. Chen, Z.G., Shi, X., Zhao, L.D., and Zou, J. (2018). High-performance SnSe thermoelectric materials: Progress and future challenge. *Prog. Mater. Sci.* 97, 283–346.
82. Serrano-Sánchez, F., Nemes, N.M., Martínez, J.L., Juan-Dura, O., de la Torre, M.A., Fernández-Díaz, M.T., and Alonso, J.A. (2018). Structural evolution of a Ge-substituted SnSe thermoelectric material with low thermal conductivity. *J. Appl. Cryst.* 51, 337–343.
83. Chandrasekhar, H.R., Humphreys, R.G., Zwick, U., and Cardona, M. (1977). Infrared and Raman spectra of the IV-VI compounds SnS and SnSe. *Phys. Rev. B* 15, 2177–2183.
84. Guo, R., Wang, X., Kuang, Y., and Huang, B. (2015). First-principles study of anisotropic thermoelectric transport properties of IV-VI semiconductor compounds SnSe and SnS. *Phys. Rev. B Condens. Matter Mater. Phys.* 92, 115202.
85. Liu, F., Parajuli, P., Rao, R., Wei, P.C., Karunaratne, A., Bhattacharya, S., Podila, R., He, J., Maruyama, B., Priyadarshan, G., et al. (2018). Phonon anharmonicity in single-crystalline SnSe. *Phys. Rev. B* 98, 224309.
86. Efthimiopoulos, I., Berg, M., Bande, A., Puskar, L., Ritter, E., Xu, W., Marcelli, A., Ortolani, M., Harms, M., Müller, J., et al. (2019). Effects of temperature and pressure on the optical and vibrational properties of thermoelectric SnSe. *Phys. Chem. Chem. Phys.* 21, 8663–8676.
87. Fauth, F., Boer, R., Gil-Ortiz, F., Popescu, C., Vallcorba, O., Peral, I., Fullà, D., Benach, J., and Juanhuix, J. (2015). The crystallography stations at the Alba synchrotron. *Eur. Phys. J. Plus* 130, 160.
88. Rietveld, H.M. (1969). A profile refinement method for nuclear and magnetic structures. *J. Appl. Cryst.* 2, 65–71.
89. Rodríguez-Carvajal, J. (1993). Recent advances in magnetic structure determination by neutron powder diffraction. *Phys. B. Condens. Matter* 192, 55–69.
90. Nevshupa, R., Martínez, L., Álvarez, L., López, M.F., Huttel, Y., Méndez, J., and Román, E. (2011). Influence of thermal ageing on surface degradation of ethylene-propylene-diene elastomer. *J. Appl. Polym. Sci.* 119, 242–251.
91. Gainza, J., Serrano-Sánchez, F., Gharsallah, M., Funes, M., Carrascoso, F., Nemes, N.M., Dura, O.J., Martínez, J.L., and Alonso, J.A. (2018). Nanostructured Thermoelectric Chalcogenides. In *Bringing Thermoelectricity into Reality* (InTech), pp. 3–22.
92. Iwanaga, S., Toberer, E.S., Lalonde, A., and Snyder, G.J. (2011). A high temperature apparatus for measurement of the Seebeck coefficient. *Rev. Sci. Instrum.* 82, 063905.
93. Quintavalle, D., Márkus, B.G., Jánossy, A., Simon, F., Klupp, G., Györi, M.A., Kamarás, K., Magnani, G., Pontiroli, D., and Riccò, M. (2016). Electronic and ionic conductivities in superionic Li4C60. *Phys. Rev. B* 93, 205103.
94. Csősz, G., Márkus, B.G., Jánossy, A., Nemes, N.M., Murányi, F., Klupp, G., Kamarás, K., Kogan, V.G., Bud'ko, S.L., Canfield, P.C., and Simon, F. (2018). Giant microwave absorption in fine powders of superconductors. *Sci. Rep.* 8, 11480.
95. Nemes, N.M.A., Alonso, J.T., Fernández-Díaz, M., Gainza, J.M., Koza, M.L., Martínez, J., and Serrano-Sánchez, F. (2019). Phonon softening and lattice thermal conductivity in SnSe thermoelectrics. temperature and dopant dependence.
96. Richard, D., Ferrand, M., and Kearley, G.J. (1996). Analysis and visualisation of neutron-scattering data. *J. Neutron Res.* 4, 33–39.
97. Bredov, M.M., Kotov, B.A., Okuneva, N.M., Oskotskii, V.S., and Shakh-Budagov, A.L. (1967). Possibility of measuring the thermal vibration spectrum $G(w)$ using coherent inelastic neutron scattering from a polycrystalline sample. *Phys. Solid State* 9, 214.
98. Marek Koza, M., Adroja, D., Takeda, N., Henkie, Z., and Cichorek, T. (2013). Vibrational Dynamics of Filled Skutterudites La T 4 X 12 ($T = \text{Fe}, \text{Ru}, \text{Os}$, $X = \text{As}, \text{Sb}$). *J. Phys. Soc. Jpn.* 82, 114607.
99. Reichardt, W. (1984). Muphocor, a Fortran program to determine the phonon density of states from neutron scattering experiments., Report no. 13.03.01p06L (Institut für Nukleare Festkörper Physik, Primärberichte des Kernforschungszentrums, Kernforschungszentrum Karlsruhe).

100. Togo, A., Oba, F., and Tanaka, I. (2008). First-principles calculations of the ferroelastic transition between rutile-type and CaCl₂-type SiO₂ at high pressures. *Phys. Rev. B Condens. Matter Mater. Phys.* 78, 134106.
101. Li, W., Carrete, J.A., Katcho, N., and Mingo, N. (2014). ShengBTE: A solver of the Boltzmann transport equation for phonons. *Comput. Phys. Commun.* 185, 1747–1758.
102. Grimme, S., Antony, J., Ehrlich, S., and Krieg, H. (2010). A consistent and accurate ab initio parametrization of density functional dispersion correction (DFT-D) for the 94 elements H-Pu. *J. Chem. Phys.* 132, 154104.